International Journal of Advanced Technology and Engineering Exploration, Vol 9(95)
ISSN (Print): 2394-5443 ISSN (Online): 2394-7454
http://dx.doi.org/10.19101/IJATEE.2021.875564

Research Article

i-Net: a deep CNN model for white blood cancer segmentation and classification

Agughasi Victor Ikechukwu* **and Murali S.**
Department of Computer Science, Maharaja Institute of Technology Mysore-571477 Karnataka, India[1]

Received: 28-February-2022; Revised: 20-October-2022; Accepted: 22-October-2022

Abstract
The immune system relies on white blood cells and platelets, which are both produced in the bone marrow and together account for around one percent of the blood corpuscles. Acute lymphoblastic leukaemia (ALL) and acute myeloid leukaemia (AML) are two major subtypes of acute leukaemia identifiable from its lineage. Unlike other chronic diseases, leukaemia is a curable blood disorder and patients' survival is possible with precise treatment. The effectiveness of this disease's treatment can be greatly influenced by early diagnosis. This study focused on a deep neural network for the segmentation and classification of ALL using the SN-AM and ALL-IDB datasets and obtained from the cancer imaging archive (TCIA) repository. ResNet-50 and VGG-19, two of the most popular deep learning networks, were used. The use of stored weights was not used for these two networks; instead, we modified the weights and learning parameters. A UNet with InceptionV2 model was used for the segmentation, while convolutional neural network (CNN) was employed to train the images after feature selection. An improved CNN called i-Net with more convolutional layers and tuned hyperparameters was proposed for the classification into normal and cancerous white blood cells. Data augmentation, dropout regularization, and batch normalization were employed to reduce overfitting. ResNet-50, VGG-19, and a proposed deep neural network called "i-Net", all have validation accuracy of 92.2%, 92.3%, and 99.18%, respectively. However, when trained without early stoppage, the model (i-Net) accuracy decreased after the 30th training cycle (epoch). CNN has shown to be accurate at diagnosing ALL according to this study. When compared to other pre-trained deep learning models such as the standard VGG-19 and ResNet-50, we achieved a better performance on the test dataset of about 630 microscopic images suggesting that the CNN can be used in clinical decision support systems (CDSS) for leukaemia detection.

Keywords
Acute lymphoblastic leukaemia, CNN, CDSS, Data augmentation, Deep learning, Image segmentation, Medical imaging.

1.Introduction
The blood, which is the lifeline of humans consists of the plasma, platelets, red blood corpuscles (RBC), and white blood corpuscles (WBC) along with another immunoglobulin. Leukaemia is a kind of blood deficiency that is usually chronic. The prevalence of leukaemia varies based on the type of disease and the demographics of the population [1]. The major cause of anaemia is blood cell proliferation, which is hindered by rapid expansion of defective blood cells [2].

Cancer of the blood primarily leukaemia, myeloma, and lymphoma with acute lymphoblastic leukaemia (ALL), a variant of blood malignancy that affects the bone marrow [1]. The term "acute" and "chronic" refers to the disease's rapid and slower progression, and if untreated at the earliest, has the potential to weaken the immune system in a short span of time. Leukaemia, the most common type of blood cancer is further divided into three, namely: L1, L2, and L3. An important plasma-rich immature teratoma that aids in the removal of infection, and three times more frequent than ALL is the multiple myeloma (MM) [4]. A decreased platelet count in the blood, a condition known as Thrombocytopenia, is a symptom of MM [5] which causes bone erosion and may be seen on CT scans as bone lesions. According to the study carried out by Ianniciello and Helgason [6], from 45 countries representing 90% of the world's

*Author for correspondence

population, it shows an increase of 3000 new cases from 53,000 cases in 2016 to 56,000 in 2020 with prevalence in Asia-pacific region representing 55% of the world's population. Similar research carried out by Liu and Long [7], reported that around 876,000 patients suffered from ALL globally in 2015 which accounts to 111,000 fatalities. Clinically, the progression of blood cancer can be influenced by so many factors such as, the patient's age, occupational hazards, progression rate, and contaminated regions, amongst others.

One of the most important elements in determining the kind of blood cancer is the blood count [8]. Manual and automated counting are also possible, and when performed by a trained person, the manual technique yields a 100% identification rate, but it is also a time-consuming operation. Automatic counting, nonetheless, is a more robust approach, but it comes with a larger chance of miscalculations. As a result, both techniques offer advantages and disadvantages.

Diagnosing leukaemia is a labour-intensive process that necessitates highly skilled medical personnel. Hence, a pathologist with extensive training in blood cell pathology must be brought in on the job. Pathologists rely heavily on medical images for diagnosis and treatment. The images are meaningless without proper interpretation, because the information is concealed in the pixels, hence requiring image processing. Unfortunately, there is a high probability that medical images may be misinterpreted due to a variety of variables, including a lack of specialists, and less attention to details [9]. There has been a lot of study done recently to automate the interpretation of medical images in order to reduce these challenges, highlighting the possibility to use computer-aided image analysis in the early diagnosis of disease [10–12]. Owing to multiple challenges in acute lymphoblastic leukaemia (ALL) diagnosis, a computer aided diagnostic system (CADS) will help the pathologist to diagnose and offer earlier treatment. Researchers have employed various deep learning models [12–14] that achieved "near-human" (expert-level) accuracy, but it is crucial to evaluate the effect different types of parameters and hyperparameters have in network training. An algorithm that uses the ResNet-50[15] and visual geometry group (VGG19) [16], a pretrained convolutional neural network (CNN) that has been fine-tuned for object categorization and detection, was used alongside a CNN model (i-Net) trained from scratch. Using both the SN-AM and ALL-IDB2 [17], we tested our methodology and found that it improved the accuracy of lymphoblast recognition compared to utilising CNNs pretrained on the ImageNet database [18]. As a result, we devised these networks in order to assess and contrast other networks based on their architectural design and parameter values.

Our contribution:

Our primary contributions are:

- An improved deep learning model for discriminating cancerous from non-cancerous microscopic images was presented.
- We presented an extension of the CNN model (Iyke-Net) proposed for pneumonia classification from chest X-ray (CXR) to the classification of WBC microscopic images.
- By modelling the architecture from the scratch, it was able to achieve promising performance accuracy. As a result, initialization weights for transfer learning were created to apply information into the WBC segmentation analysis.
- Using a fine-tuned, pre-trained model, we achieved a level of accuracy that is on par with most state-of-the-art methods.

This manuscript is subdivided into 6 sections. Section 1 highlights the background, and aim of the study. In section 2, we presented a review of the work on leukaemia classification from microscopic images using deep learning approaches. A detailed description of the materials and methods is presented in section 3. The experimental findings and comparison of existing models were addressed in section 4. Section 5 highlights the discussion and limitations of the research. The conclusion and future directions were discussed in section 6.

2.Literature review

In medical image processing, pre-processing and feature extraction are of prominence in the segmentation and classification phases of contaminated blood cell image analysis. The works of [19–21] on the microscopic images of patients with B-lineate ALL yielded the famous SN-AM dataset consisting of 30 images, in which one image served as point of reference, 29 others used to test the suggested stain normalization method. Based on image analysis, Foran et al. [22], offered a clinical decision support system for discriminating between different hematologic malignancies that allowed image analysis with the "gold standard" dataset and recommendations based on a large number of cases with an accuracy greater than 83%. The authors employed data augmentation, followed by

normalizing the training data prior using a CNN architecture for categorization. Originally, the dataset was enhanced for identifying acute myeloid leukaemia by employing numerous changes such as histogram equalization. To categorize ALL from microscopic blood samples, Rehman et al. [23], trained a robust CNN model from bone marrow images and achieved classification accuracy of 98%. Convinced by their findings, the authors proposed similar architecture for the classification of ALL. Using images of bone marrow, Markiewicz et al. [24], proposed an approach for classifying 17 kinds of blood cells in myelogenous leukaemia. Their method worked well for differentiating the most salient distinctive features before final classification with support vector machines (SVM). Shafique and Tehsin [25], employed a deep CNN for the classification of ALL into various subgroups namely, L1, L2, and L3. A method to reduce overfitting called data augmentation was used and an accuracy of 96.06% was attained for the sub-types' classification. In a leukaemia image slide, Abd et al. [26], suggested an automated method for identifying the number of cells infected with leukaemia. To remove background white blood cells, hue, saturation, and value (HSV) segmentation was utilized, followed by morphological erosion, to remove cells that overlapped. The segmentation of colour smear of microscopic images using the H component of the hue, saturation, and intensity (HSI) colour space containing information about white blood cells was explored by Wu et al. [27], using an iterative Otsu's method highlighting "S" component which provides information on the nuclei of cells. A thresholding technique for leukaemia detection using blood ratio was investigated by Salihah et al. [28], where the ratio of blood cells for leukaemia detection was calculated using the number of counted blood cells. To improve computational time, few pre-processing and post-processing techniques were also used. The result revealed that the blood cell ratio determined using the proposed image processing algorithms distinguished between normal and abnormal blood cells. Horie et al. [29], showed the robustness of deep neural networks such as CNN for oesophageal cancer, with a sensitivity of 98 percent for squamous cell carcinoma and adenocarcinoma. It was Saba et al. [30], who suggested a cascaded architecture for skin lesion identification that included three key steps: contrast and boundary extraction with CNN, followed by feature extraction with transfer learning. An entropy-controlled feature selection approach was presented, highlighting that their approach was robust with 98.4 percent accuracy on the PH2 dataset. Shekaran et al. [31], suggested a CNN to discriminate between infected and uninfected images. Zuluaga-Gomez et al. [32], suggested hyperparameter-fine-tuned computer-aided diagnostic systems for categorization of thermal images using a CNN. Using an optimization method with a tree-based discriminator, false-positive and false-negative classification rates was reduced considerably. A fine-tuned CNN model called Iyke-Net was proposed by Ikechukwu et al. [33], for the training and categorization of pneumonia and normal chest X-ray images. With a recall of 92.03%, the pre-trained model yielded better results when compared to a model trained from scratch. The works of Dabeer et al. [34] offered a method for classifying mammographic images with a densely connected network, which recorded an accuracy of approximately 100%.

In a study by Ahmed et al. [35], a new strategy for reducing noise from microscopic blood cells on the ALL-IDB and ASH image bank databases, both of which are open to the public was proposed. The CNN model's performance was found to be 88.25 and 81.74 percent, respectively, for the ill and healthy groups. The CNN model outperforms other common machine learning algorithms in their study. Genovese et al. [36], presented the first histopathological transfer learning method for detecting leukaemia-related lymphomas. For the purpose of identifying diseased tissues, techniques were developed employing CNNs trained on a histopathology database. When trained on the ImageNet database, CNNs was able to recognize lymphoblasts more accurately than those trained on the ALL-IDB2 dataset. The works of Zolfaghari and Sajedi [37], focused on the classification of ALL and WBCs from microscopic images. Detailed survey was presented on most articles published in the same domain. It was observed that diagnosis of acute leukaemia has generated a lot of attention and many scholars have employed deep neural networks for the same. The use of hypercomplex-valued network (HVN) was investigated by Vieira and Vale [38], using 8 complex-valued CNN. Analysis showed that their proposed hypercomplex CNN produced commendable results at 96.6% when tested on ALL-IDB2 dataset using 50% of the data for texting. Kasani et al. [39], employed data augmentation and transfer learning. This approach was adopted to increase the sample size of the dataset that made the model more generalizable. Results showed that their approach was better at discriminating diseased and healthy cells. Bodzas et al. [40], proposed an

approach based on human visual perception with the implementation of three-phase filtration algorithm for segmentation. A combination of SVM and neural nets had a specificity of 95.31 percent, and sensitivity were 98.25 and 100 percent, respectively. A fused approach involving UNET and deep CNN was employed by Alagu [41]. The dataset used was obtained from the ALL-IDB2 and resized to a uniform dimension. Statistical analysis yielded a p-value of 0.00001, an improvement over classical methods suggesting that the methodology can help in clinical decision support systems. Fouladi et al. [9], applied deep neural networks in the diagnosis of COVID-19 from CT scan images using two pre-trained networks. With accuracies above 90%, it could be inferred that pretrained networks were better at discriminating important features from biomedical images. Similarly [42–43] used ensemble learning approaches to classify ALL from microscopic images. Data enhancement method for random sampling was employed to address the issue of data imbalance. An accuracy of 99.03% proved that ensemble approach was better than classical methods.

Based on the existing literature, it was observed that numerous works has been done using datasets obtained from ALL-IDB2 repository. Traditional approaches such as K-Means, Fuzzy C-Means clustering and SVM has achieved accuracies closer to the state-of-the-arts model. However, deep learning models always outperform classical machine learning owing to a greater number of hidden layers and the choice of hyperparameters. Data augmentation, dropout regularization and ensemble approach constantly yield better accuracies, suggesting that deep CNN is a de-facto standard for medical image analysis.

3.Methods

3.1Dataset description

For this research, we combined data from two separate sources. The first dataset is called SN-AM retrieved from the cancer imaging archive (TCIA) repository. It has 100 images of MM and 90 images of B-ALL with enough variation between them. At 1000x magnification, using a Nikon Eclipse-200 microscope fitted with a digital camera, Duggal et al. [20], acquired the images in a raw BMP format at a size of 2560×1920 pixels. There is a total of 30 images in the collection, with a single image serving as the gold standard. These 30 images were accompanied by two more images, one showing the nucleus mask and the other the background mask as shown in *Figure 1*. The second dataset is the ALL-IDB2. IDB1 and IDB2 are two distinct datasets that can be found in the ALL-IDB database. The ALL-IDB2 version 1.0 is a compilation of normal and blast cells' cropped areas of interest from the ALL-IDB1 dataset. Images from the ALL-IDB2 have the same grey level characteristics as images from the ALL-IDB1, with the exception of the image size. Since the ALL-IDB2 dataset was created to evaluate the effectiveness of classification systems, we used it to test our method. ImXXX Y.jpg is the first character in the names of the ALL-IDB2 picture files. XXX is a progressive 3-digit integer, Y is a boolean digit that is equal to 0 if the cell placed in the image's centre is not a blast cell and equal to 1 if it is.

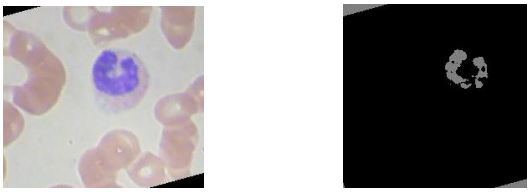

Figure 1(a) Input image (b) Input mask

Data augmentation was employed to obtain a total of 3102 microscopic images in both the training and testing folders, corresponding to 1650 healthy cells and 1,452 leukaemia cells saved in two separate folders as normal and cancerous, shown in *Figure 2.*

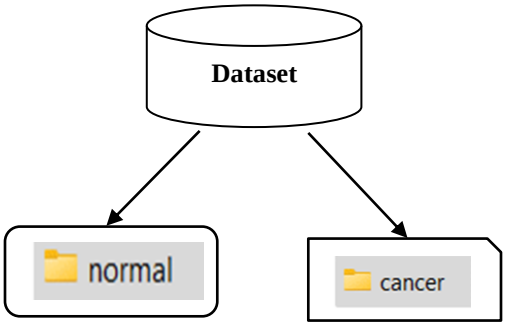

Figure 2 Distribution of the ALL dataset

i) *Data Augmentation:* The absence of enough data is one of the most frequently occurring issues that arise during the implementation of machine learning in the workplace. This is due to the fact that the collection of such data can frequently be both time-consuming and costly. A collection of strategies known as "data augmentation" was implemented in order to enhance the sample size. These strategies involved the creation of additional data points using the already collected data. The SN-AM dataset contributed by [18–21] was initially supplemented by translating and rotating the images as shown in *Table 1.* Model training and validation sets were created from the

jumbled images while ensuring that variation in sizes, postures, and lighting settings was addressed to generalize well during model evaluation. Thus, additional images were created from the existing dataset by using different image manipulation techniques. The parameters chosen are highlighted in *Table 1*.

Table 1 Framework for data augmentation

Method	Default	Adjusted
Horizontal flip	None	True
Rescale	-	1.0/255
Zoom range	-	0.25
Rotation (Degrees)	-	30, 45 & 60
Fixed image size	1024×1024	224×224

Firstly, we rotated the images by 30, 45 and 60 degrees respectively as shown in *Figure 3(a), (b)* and *(c)*. These approaches proved helpful in handling over-fitting, thereby making it easier for the model to generalize to new cases outside of the training set.

3.2ResNet-50 and VGG-19:

Residual neural network (ResNet) was initially proposed by the Microsoft research team in early 2015, consisting of 50 deep convolutional layers. A pretrained version of the network can be found in the ImageNet database, trained on images greater than one million. It is about 6 times deeper than VGG-19 and regarded as the deepest neural network at that time. It yielded the best classification result in the ILSVRC 2015 competition, an approach that made it possible to rank first place in a number of other categories as well. Since ResNet-50 and VGG-19 are closely identical in terms of the number of hidden layers, we will discuss the architecture of ResNet-50, better explained in the works of Wang et al. [44], and depicted in *Figure 4*.

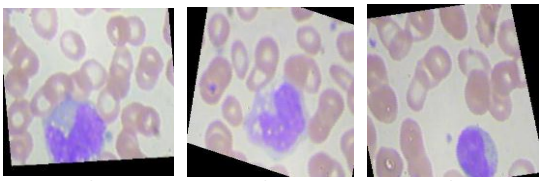

3(a): 30° 3(b): 45° 3(c): 60°

Figure 3 Data augmentation highlighting rotations at 30, 45 and 60 degrees respectively

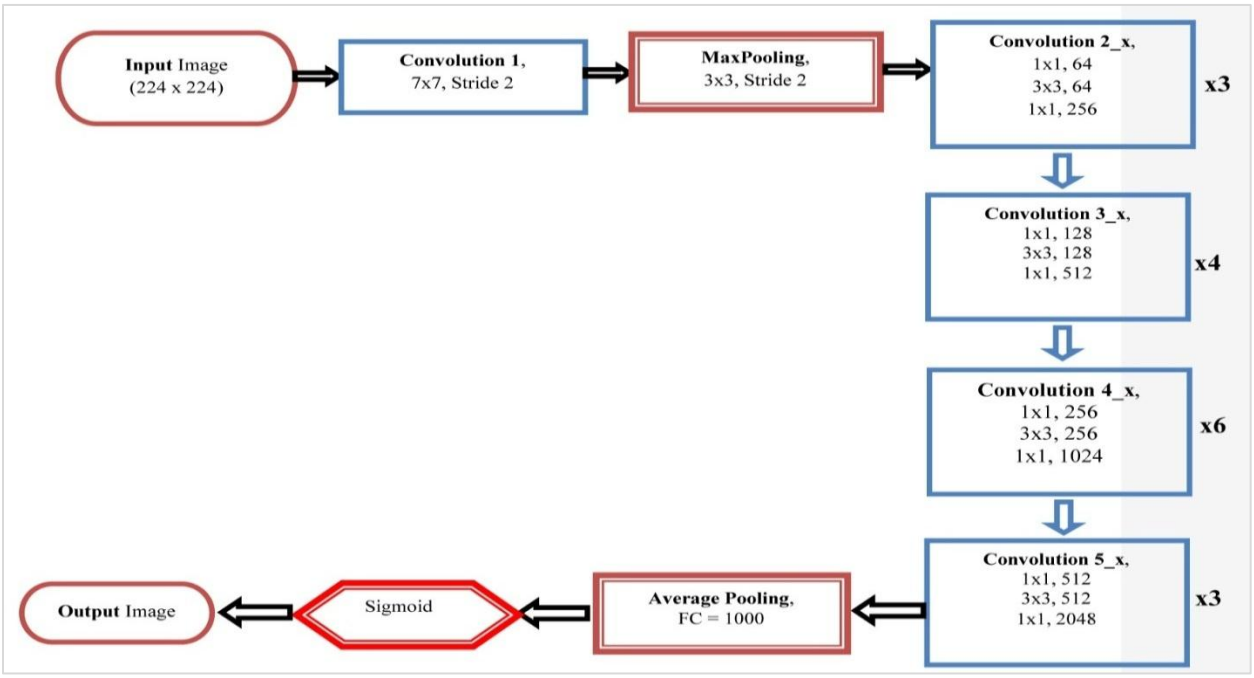

Figure 4 ResNet-50 architecture with different stages and FC-Block

Identity blocks are shown as "ID BLOCK" in the diagram, and "ID BLOCK × 3" refers to stack three identity blocks. Between the input and output, layers are 4-stages with one fully-connected layer.

i) Stage 1: There are two-dimensional (2D) convolution of dimension (7×7) with 64 filters. Batch normalization and pooling (Max-pooling) was applied using a stride length of 2.

ii) Stage 2: This convolution stage uses three sets of filters of sizes (32, 32, 64), a stride length of 2 and a max-pool layer.
iii) Stage 3: This consists of two blocks with three sets of filters of size (128, 128, 512). Batch normalization with rectified linear unit (ReLU) is designated as "B" and "BA" respectively.
iv) Stage 4: At this layer, the identity block consists of filter sizes (256, 256, 1024), with only two blocks.
v) Stage 5: The last stage is the fully connected layer, followed by average pooling and flatten layer for classification. This layer does not contain any hyperparameters.

The ResNet-50 is a type of pre-trained CNN that is 50 layers deep. It consists of 48 convolutional layers, with one max-pooling and average-pooling layers respectively. Input image of dimension 224 by 224 is fed as an input which is first passed through a convolutional layer with a filter of 7×7, and a stride length of 2. Max-pooling operation is performed next, followed by series of convolutional operations that employs 3x3 kernel sizes. At the end of the fifth convolutional layer, summation of all pooling operation, called "average pooling" is performed. Subsequently, a sigmoid activation function is applied to "squash" the probability between 0 and 1 on the final output image. These set of operations ensures the output image is not overfitted.

3.3Preprocessing of images

Two approximately processed images are used for additional processing in this stage. We begin by converting the colour image to grayscale. The contrast was adjusted using the alpha (α) and beta (β) values, often called the gain and bias parameters expressed as Equation 1.

$$g(i,j) = \alpha \times f(i,j) + \beta \quad (1)$$

OpenCV inbuilt methods cv2.convertScaleAbs(), already implements this along user defined alpha and beta values. *Figure 5* shows the grayscale and contrast-enhanced images used to categorize the pixels. The global contrast stretching (GCS) method was used to boost the contrast of the image. GCS is done by moving a sliding window across the image and changing the middle pixel element according to Equation 2.

$$I_{(a,b)} = \frac{255 \times |I_a(a,b) - x|}{(y-x)} \quad (2)$$

Where: $I_{(a,b)}$ represents the output colour level for the image pixel coordinates. (a,b), $I_{a\,(a,b)}$, the input colour level for the pixels (a,b); y & x are the maximum and minimum values respectively.

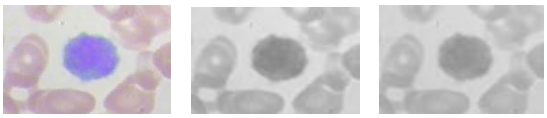

(a) (b) (c)

Figure 5 (a) input image, (b) grayscale image and (c), contrast-enhanced image

The adjusted data produced after feature selection was first normalized using the ImageDataGenerator with a shear range of 20%, subsequently resized to 224×224, then shuffled into training, test and validation sets with 60% for training, 10% for testing and 10%, for validation. The remaining 20% was reserved as "unseen dataset", an approach that was investigated in our study. Subsequently the images were rotated by 30, 45 and 60 degrees respectively as shown in *Figure 3(a), (b)* and *(c)* to ensure the model recognizes the images in various orientation. These approaches proved helpful in handling over-fitting, thus making it easier for the model to generalize to new cases outside of the training set.

3.4CNNs

Given that our solution relies on a deep neural network, we detail how it works. CNNs are class of neural networks that has found useful application in image classification and machine vision.

There are three primary layers in a CNN, namely: a convolution layer, an aggregation layer, and a completely linked layer. The image is passed to the convolution layer, which contains neurons that function as feature extraction units. An activation map is created by convolving a filter, $f \times f$ matrix with the input images; stride $length$ is the constant amount which advances the filter along the images. Convolution performed on an image of $m \times n$ using a filter fr, padding pa, and stride sr yields the corresponding image (Equation 3).

$$(Oimg) = (m - fr + 2pa)/(sr + 1) * (n - f + 2pa)/(sr + 1) \quad (3)$$

In addition, the filter's depth is determined by the type of images utilized for training. The standard SoftMax $\sigma_{(xa)}$was used to introduce nonlinearity to the model defined as (Equation 4):

$$\sigma_{(xa)} = \frac{e^{xa}}{\sum_{b=1}^{n} e^{xa}} \quad (4)$$

for a $= 1, \ldots, n$; x $= (x1, x2, \ldots, xn) \in \Re^n$
Where n = the sum of elements of the input vector x
for a $= 1, \ldots, n$; x $= (x1, x2, \ldots, xn) \in \Re^n$
Where n = the sum of elements of the input vector x

3.4.1 Convolutional layer:

The introduction of non-linearity is an essential idea in CNNs. This model employs the non-linear function of the max-pool layer which ensures that maximum value of non-overlapping regions was selected. The maximum value of any region of interest in the image of $m * n$ dimension, described by a kernel function k and stride size sr, is extracted using max-pooling operation: $\frac{m-k}{sr+1} \times \frac{(n-k)}{sr+1}$. A max-pooling layer down samples the given image, as seen in *Figure 6*.

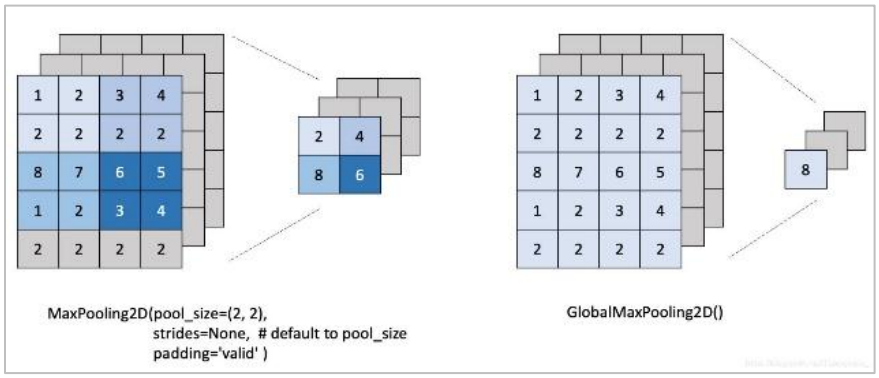

Figure 6 Maxpooling function on convolved image

3.4.2 Fully Connected layer:

The name "totally connected" comes from the fact that a completely linked layer binds every neuron to another. They work like regular neural networks, classifying images using the convolved features. At this point, loss functions are computed and then backpropagated. The proposed model is comprised of five interconnected layers, the fifth of which is the output layer. All four interconnected layers utilize SoftMax as their activation function. The sigmoid activation function defined in Equation 5, produces a probability in the range of 0 and 1 for each independent class label the model aims to predict according to Equation 5.

$$Sign(x) = \frac{1}{1+e-x} \quad = \frac{e^x}{1+e^x} \qquad (5)$$

Where x=input vector

3.5 Segmentation using UNet:

The UNet has found useful applications in computer vision in which white blood cell nuclei may be precisely segmented, which aids in the detection of the alterations seen in people with ALL. With U-Net, we were able to isolate the nucleus from both normal and cancerous cells, then applied upsampling to output the final image.

The architecture of UNet model is as shown in *Figure 7*.

A narrowing path and an expanding path make up the U-Net structure. The inducing route is a common convolutional network, with convolutions followed by a ReLU and a maxpooling operation. The process of compression results in a reduction in the amount of space available, and an increase in the number of available features. The high-resolution features from the contracting path are included into the expansive pathway via a series of upsampling that preserves the feature and spatial information. Upsampling typically involves a transposed convolutional layer, and the resulting feature map has a higher spatial dimension than the original feature map. In order to increase the precision of the segmentation process, the concatenation operation is helpful since it fills the gap in the positional data for the pixels that were lost during the convolution step.

The input image was that of microscopic images of both normal and masked cells as depicted in *Figure 8*. The respective binary images were first resized to 224×224, and trained for about 30 epochs. Accuracy and receiver operating curve (ROC) performance measures were used alongside the corresponding ground truth to validate the results.

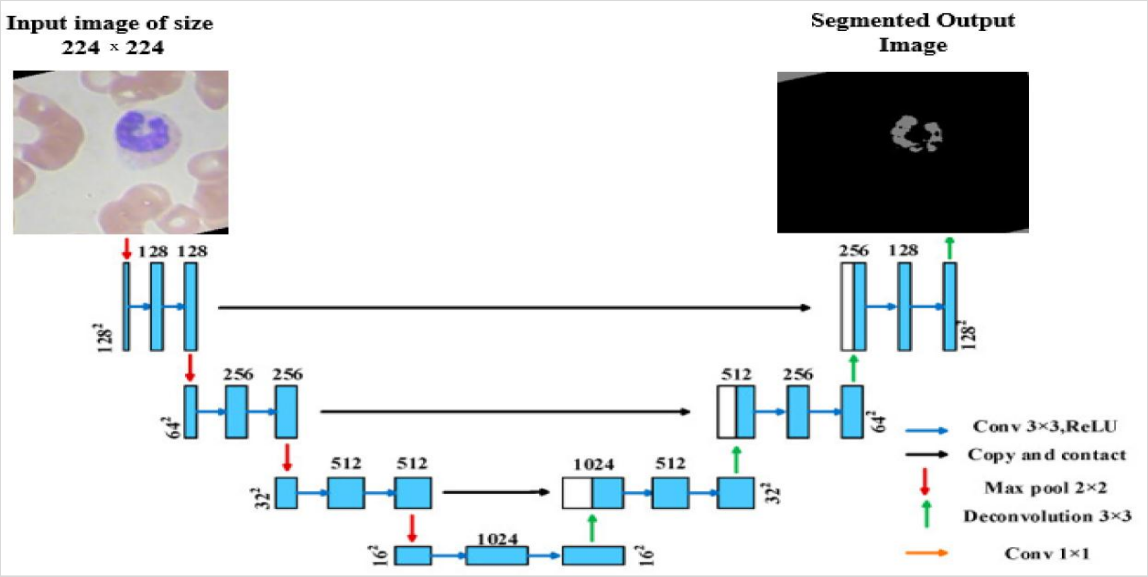

Figure 7 UNet architecture for semantic segmentation

Figure 8 (a) Normal image (b) Masked Image

3.6 Proposed deep neural network model

An improved CNN model (i-Net) for cancer type categorization (such as ALL) was implemented. It employs a minimal amount of pre-processing in contrast to other image categorization methods. The model takes an input image and predicts the cancer type as an output. The fundamental CNN consists of 5 convolution layers, fully connected and dense layers with varying dropout regularizations. The technique is based on training a CNN for leukaemia classification using images obtained from the TCIA database, replacing the last fully-connected layer with a layer designed for detecting pneumonia from chest-x-ray (CXR) images, followed by fine-tuning the resulting CNN for ALL detection. The resulting CNN is referred to as i-Net in the remaining sections of the paper. Our method involves the following approaches as shown in *Figure 9.*

For classification, the convolution layers of 128, 64, 32, 16, and 8 filter lengths were included in the network, as well as two convolution layers of size 64. Kernel function *2×2* was used for all the layers. The *2×2* max-pooling layer is considered with stride length of 2 in this architecture. A flattened layer takes the 2D output of the final pooling layer and converts it to a 1D layer. All convolution layers utilize the same padding. Using a 1024 fully connected layer, a SoftMax activation function was used to categorize data into two classes (normal and leukaemia). Batch-normalization layers was evaluated after all the convolution and dropout layers with rates of 0.2, 0.25, 0.35, and 0.45 respectively in order to prevent overfitting the model as illustrated in the algorithm and accompanying *Table 2*. The optimization function, Adam was used, which has a learning rate of 0.0001.

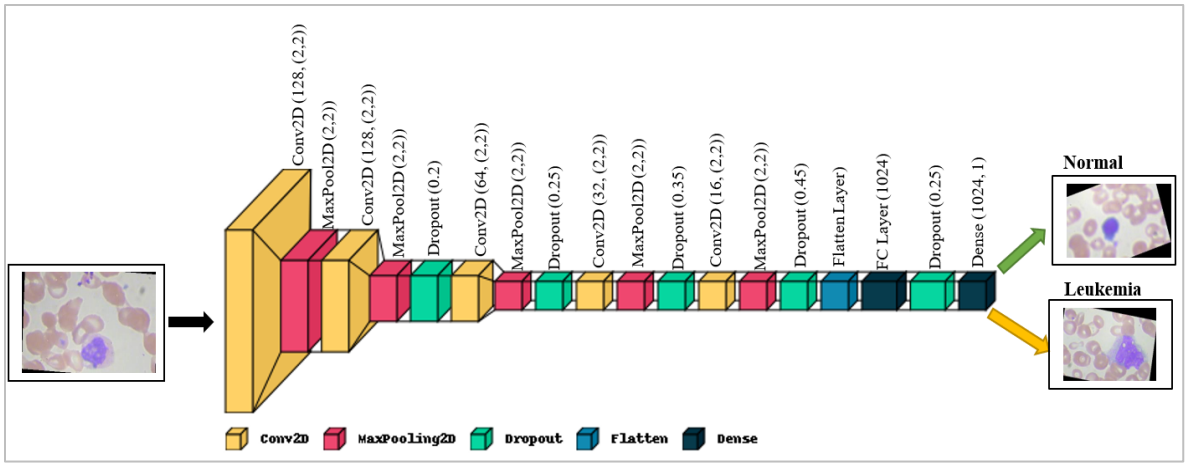

Figure 9 Proposed deep neural network (i-Net)

Algorithm for the proposed model (i-Net) for WBC classification:

Begin Procedure LoadImages(datasets)
for every x in datasets (SN-Am, ALL-IDB2) **do**
resize the input image (224 x 224 x 3)
do:
find the countours
apply data augmentation (30^o, 45^o, 60^O)
normalize the images (imgPixels / max(255))
end do
find subclass(dataset)
if "Normal" in subclass, **then:**
return 0
otherwise:
return 1 (Cancerous)
end if
end find
sub-procedure segmentation(dataset)
for every image in normalized images:
apply UNet model
select region of interest
end for
forward to the proposed model(i-Net):
do:
1.create sequential model
2. add convolution, maxpooling layer
3.activation(relu)
4.padding(same)
dropout (20%)
repeat steps 1,2,3 and 4
dropout (25%)
repeat steps 1,2,3 and 4
dropout (25%)
repeat steps 1,2,3 and 4
dropout (35%)
Add **flatten** and dense **layers**
dropout (40%)
add dense(1) and activation (softmax)
end **forward**
end sub-procedure
procedure classify (testImages)
if argmax() prediction < 0.5 then

```
                    classify = 0 (Normal)
            otherwise:
                    classify = 1 (Cancerous)
            end if
        end procedure
end Begin procedure
```

Table 2 Table of values for the input and output layers

Layer (type)	Output Shape	No. of Parameters
conv2d_16 (Conv2D)	(None, 32, 32, 64)	3316
max_pooling2d_16(MaxPooling2D)	(None, 16, 16, 64)	0
conv2d_17 (Conv2D)	(None, 16, 16, 64)	65600
max_pooling2d_17(MaxPooling2D)	(None, 8, 8, 64)	0
dropout_12(Dropout)	(None, 8, 8, 64)	0
conv2d_18(Conv2D)	(None, 8, 8, 128)	131200
max_pooling2d_18(MaxPooling2D)	(None, 4, 4, 128)	0
dropout_13(Dropout)	(None, 4, 4, 128)	0
conv2d_19 (Conv2D)	(None, 4, 4, 128)	262272
max_pooling2d_19(MaxPooling2D)	(None, 2, 2, 128)	0
dropout_14(Dropout)	(None, 2, 2, 128)	0
conv2d_20(Conv2D)	(None, 2, 2, 128)	262272
max_pooling2d_20 (MaxPooling2D)	(None, 1, 1, 128)	0
dropout_15(Dropout)	(None, 1, 1, 128)	0
flatten_3(Flatten)	(None, 128)	0
dense_19(Dense)	(None, 256)	33024
dropout_16(Dropout)	(None, 256)	0
dense_20 (Dense)	(None, 1)	257

Total params: 757,761
Trainable params: 757,761
Non-trainable params: 0

Data was sent to the network in batches of size 32 after the network has been trained for 30 epochs using Keras and Tensorflow libraries. Research in this study was conducted on Google Colaboratory (Colab), a free open-source library for training deep learning models to discriminate salient features for the classification of cancerous images.

The effectiveness of our approach was verified on the publicly available SN-AM dataset, which proves to be more accurate on large datasets.

3.7 Performance metric:

The performance of the proposed model (i-Net) for discriminating cancer and non-cancerous images, was evaluated using standard metrics expressed mathematically as in Equations 6 to 10. The accuracy of ALL (Acc_all) is defined as the number of instances rightly classified to the sum of instances. This is expressed in Equation 6:

$$Acc_{\_all} = \frac{TP_{all} + TN_{all}}{TP_{all} + FP_{all} + TN_{all} + FN_{all}} \quad (6)$$

Precision, commonly called the positive predictive value represents a portion of instances that were truly classified as represented in Equation 7:

$$Prec(PPV)_{\_all} = \frac{TP_{all}}{TP_{all} + FP_{all}} \quad (7)$$

The sensitivity assesses the model's capability to identify positive samples in a dataset. The greater the recall, the greater the number of positive samples found, expressed mathematically in Equation 8:

$$Sens(Recall)_{\_all} = \frac{TP_{all}}{TP_{all} + FN_{all}} \quad (8)$$

In Equation 9, the model's specificity measures how many true negatives it accurately predicts.

$$Spec_{\_all} = \frac{TN_{all}}{TN_{all} + FP_{all}} \quad (9)$$

F1-score or the F-measure is the harmonic mean of the model's precision and recall. This is illustrated in Equation 10.

$$F1 - Score_{\_all} = 2\left(\frac{Prec_{all} * Sens_{all}}{Prec_{all} + Sens_{all}}\right) \quad (10)$$

4. Results

The purpose of this research was to propose practical characteristics of healthy and infected cells for ALL detection. The research takes into account 1650 images of normal cells and 1452 images of cancer cells from the publicly available SN-AM and ALL-

IDB2 repository. The results of pre-processing alongside segmentation and ground truth validation are highlighted in *Figure 10.*

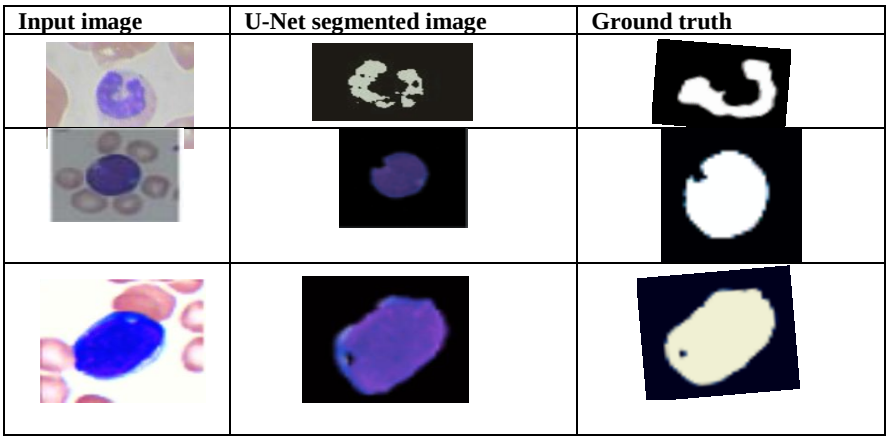

Figure 10 Results of segmentation and ground truth validation

TensorFlow, an open-source python framework was used to create the classification model. Followed by a binary classification after 30 epochs. Each cycle uses the Adam optimizer as the loss function, resulting in the smallest loss in the end. Owing to limited computational resources, the model was trained on the collab, a freely available development environment powered by Google graphics processing unit (GPU) and tensor processing unit (TPU) that gives researchers easy access to collaborations. *Table 3* suggested that our proposed CNN approach was better at classifying normal and cancerous microscopic images.

Table 3 Model performance metrics on both datasets

SN-AM	**#Epochs**	**Training Acc. (%) VGG-19**	**Training Acc. (%) ResNet-50**
	10	86.2	89.1
	20	89.5	88.1
	30	90.1	89.3
	50	89.5	90.1
	70	92.1	89.8
	90	**92.3**	**90.2**
ALL-IDB2	**#Epochs**	**Training Acc. (%)**	**Validation ACC. (%)**
	10	89.1	87.2
	20	90.2	88.1
	30	90.5	89.2
	50	86.2	89.2
	70	90.9	90.1
	90	92.2	**90.2**

*Note: **Bold** figures indicate best performance metrics (Accuracy)

Stochastic gradient descent (SGD) was used to train all models over the course of 30 iterations. For ResNet-50 and VGG-19, the starting learning rates were set at 0.001 and 0.01 respectively. The initial learning rate for i-Net was set to 0.001, and on epochs 30 and 40 it was dropped by a factor of 10. All models had their momentum and decay set to 90% and 0.000001, respectively. For training, there are two options: (1) fixed, where convolution filters cannot be trained after initialization, and (2) trainable, where filters can be trained to the best representation. As seen in *Figure 11*, CNN performs

badly in the first scenario after the 25th epoch. This is as a result of the model being overfitted and our failure to implement an early stopping. However, on the second 'trainable' option, where filters and other hyperparameters were adjusted, a noticeably greater test accuracy is obtained. For the VGG-19 and ResNet-50 results prefixed with the trainable layer in the last row, we used a 5-fold cross validation method. For the VGG-19 on the SN-AM dataset, we observe a considerable increase in training accuracy, from 89% to 92.2%. Similar improvements were seen on the ALL-IDB2 dataset up to the 90th epoch. The behavior accounted for since both pre-trained models are similar in the architecture as shown in *Figure 11*. When we extended the training to the 90th epoch, the accuracy of the training increased from 89% to 91%.

Table 4 suggested that our proposed CNN approach was better at classifying normal and cancerous microscopic images with limited computational resources.

In the proposed model, we employed variations of data-augmentation, dropout and batch normalization techniques as explained in the discussion section

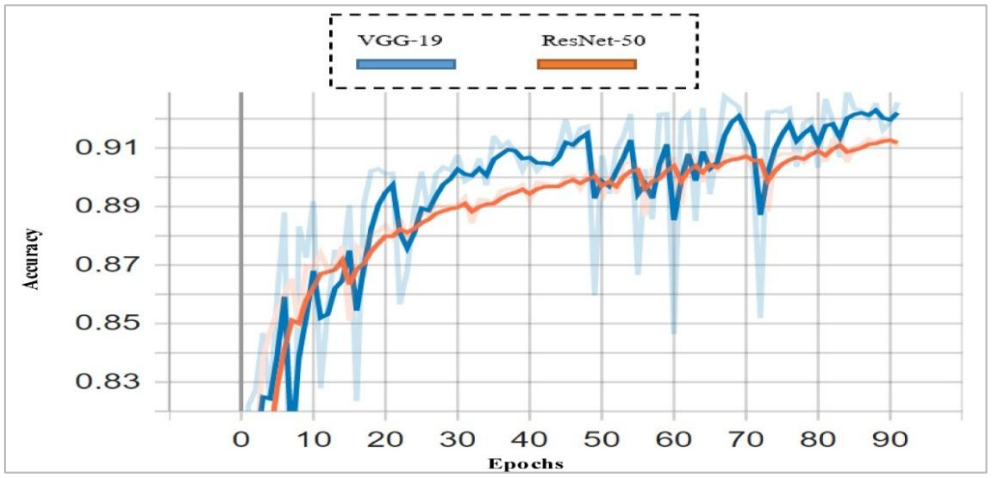

Figure 11 Results of training and validation accuracy on SN-AM and ALL-IDB2

Table 4 Model accuracy (Acc.) for proposed model (i-Net)

Epochs	Training Acc. (%)	Validation Acc. (%)
5	80.20	80.20
10	95.00	90.00
15	97.20	96.00
20	93.20	88.20
24	**99.60**	**99.18**
25	78.00	78.00
30	90.00	91.00

*Note: **Bold** figures indicates best performance metrics (Accuracy).

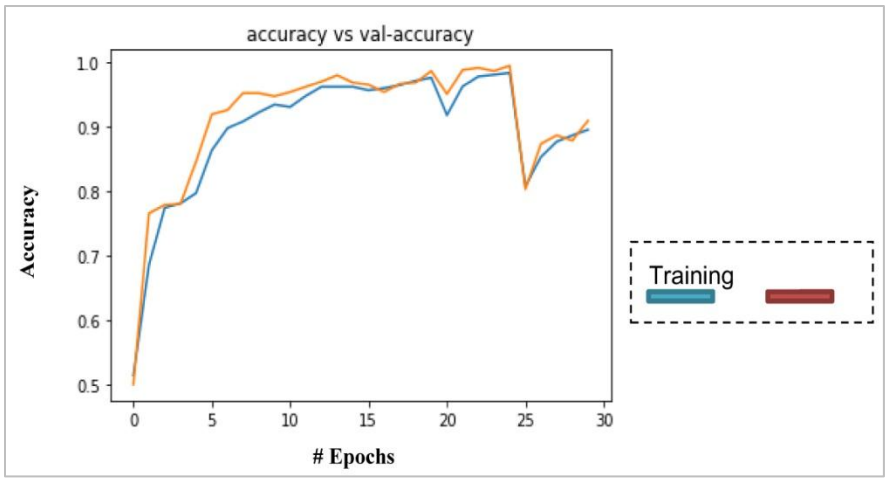

Figure 12 Training vs validation accuracy

5. Discussion

The entire ALL dataset was then divided into thirds: 60% for training, 10% for validation, and 10% for testing and another 20% was reserved, called "unseen" data. Each i-Net is trained for 30 iterations using a stochastic gradient descent on the training portion of the SN-AM dataset, using the following parameters: batch size of 32, learning rate (LR) of 0.0001, and momentum (M) of 0.9. After 24 iterations, the learning rate was adjusted to 0.00001. The strategy employed to verify if the accuracy of the proposed network can be further increased, which turns out to be the opposite. We use a deep tuning strategy to fine-tune the network, allowing gradient update on all weights of the CNN rather than just the final fully-connected layer. The weights for each i-Net are chosen based on their ability to produce the best classification accuracy on the training set, and subsequently applied to the testing set of the SN-AM dataset, from which the error measures are calculated. All of the i-Net accuracy across the various epochs is as detailed in Table 4. It was observed that accuracy did not improve after the 24th epoch. Using the early stoppage technique, training was halted when the accuracy did not improve beyond 99.18%, a behaviour shown in *Figure 12.* Subsequently, the model was able to discriminate cancerous from normal microscopic cells when deployed as shown in *Figure 13.*

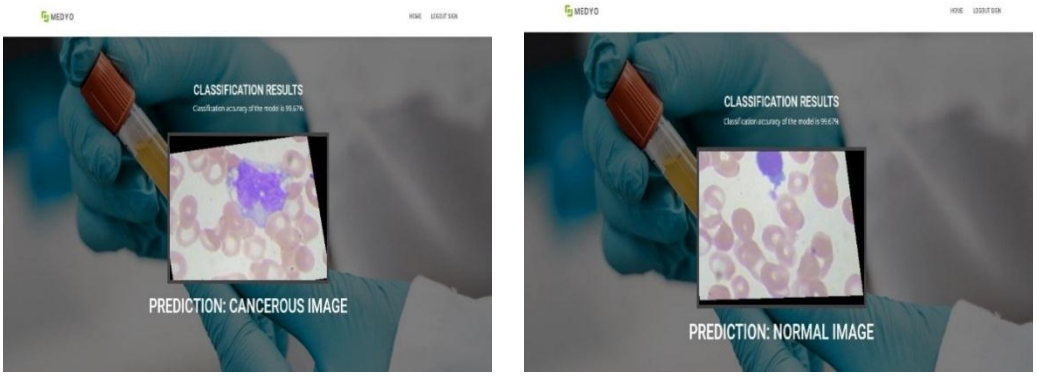

Figure 13 (a) Cancerous image (b) Normal image

One way to visualize how well a classification model performs across different cutoff points is through an ROC. The two variables shown by this curve are: true positive rate (TPR) and false positive rate (FPR) as explained in equations 6 to 8. On a ROC curve, TPR and FPR are displayed against one another for a variety of categorization criteria. When the threshold for positive categorization is lowered, a greater number of objects are labelled as positive. This results in an increase in the frequency of both false positives and true positives. The accompanying *Figure 14* provides a representation of a typical ROC curve.

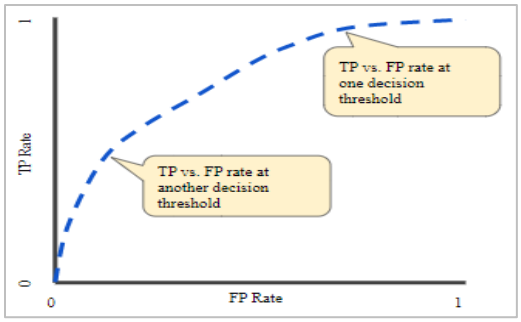

Figure 14 Typical ROC curve

The proposed model's ROC curve is shown in *Figure 15*. An evaluation using the TPR was done against the FPR to construct the ROC curve (FPR). Since comparing curves is extremely difficult, we define an ideal test case for accuracy and recall curves further towards the top right corner. For each conceivable cutoff, *Figure 15* depicts the connection between accuracy and recall. Our classification findings, as shown in *Figure 12*, tends to the ideal case of the ROC curve. Further analysis done using pre-trained models suggested that our model outperforms transferred learning approaches like VGG-19 in terms of accuracy, with the goal of reducing computing costs considerably. Simonyan and Zisserman [45], in early 2014 proposed the famous VGG network which was trained on the ImageNet ILSVRC dataset consisting of 1.3 million images using SoftMax as the classification algorithm (Yu et al., 2016).

Validation Sets: A comparative analysis was presented in *Table 5* against existing state-of-the-arts techniques, used as "ground truth" in most situations.

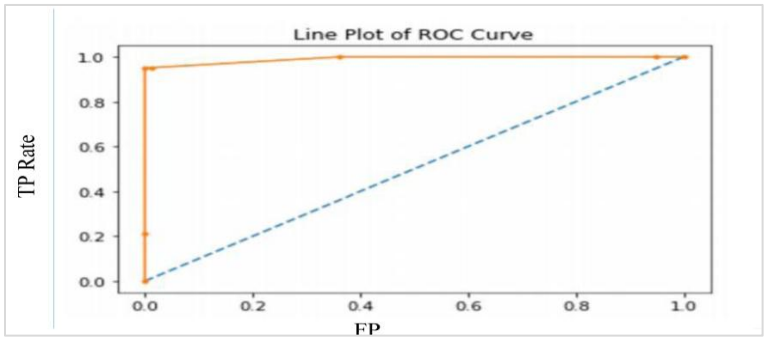

Figure 15 Line plot of the model's ROC curve

Table 5 Performance comparison with existing methods

Related works	Models	Accuracy (%)	F1-value (%)	Precision (%)	Recall (%)
[46]	ChexNet	85	95	-	-
[47]	ResNet-50	84.5	-	-	0.10
[48]	VGG-19	93.5	-	-	86.0
[49]	Alexnet	96.5	-	-	-
[50]	Xception	93.90	-	-	-
Proposed method	Proposed (**i-Net**)	**99.18**	**99.19**	**99.30**	**99.18**

The effectiveness of the proposed deep learning technique in comparison to previous efforts. The proposed method outperforms competing approaches, with an accuracy of about 3%. As can be shown in *Table 5*, the overall accuracy of 99.18% and the ability to distinguish cancer cells from normal cells are both enhanced by the selection of hyperparameters and fine-tuning features. At the twenty-fourth epoch, the accuracy of the classification was found to be quite high as compared to earlier approaches.

5.1Limitation

The lack of expensive computational resources made us limit the size of the dataset to about 3102 microscopic images. Although, it has more convolution layer than normal CNNs, the network (i-Net) will take a little less time to implement in systems with basic configurations. Further, our proposed convolutional network's validation accuracy was better than VGG-19 and ResNet-50, despite only being tested on a small dataset. Its simpler architecture and faster execution time will lead to its use being explored further. We did not investigate segmentation approaches for myeloma and non-

myeloma as we focused only on ALL. A complete list of abbreviations is shown in *Appendix I.*

6. Conclusion and future work

In this paper, we demonstrated the ability of training a deep convolutional network for the segmentation of WBC cells from microscopic images with comparable accuracy on the freely available GPU on Google colab. Our method was able to distinguish key elements that aided in discriminating cancerous white blood cells from microscopic images. For the previously indicated aim, a new CNN model was proposed. We were able to achieve 99.18 percent training accuracy through variations of hyperparameter optimization, 84.5 percent for ResNet-50, and 93.5 percent for VGG-19. The results show that these techniques can improve classification accuracy and precision. Our tests revealed that our model can generalize to new datasets, which is an important step toward developing a reliable computer-assisted diagnostic tool. However, it was observed that for deep neural networks to reach state-of-the-art accuracy, extensive experimentation is required. Furthermore, the size of the dataset chosen was smaller compared to those used in pre-trained models. It is common for pre-trained networks to be slow to run, yet our proposed model was better and produced promising results despite its simplistic architecture. We only used a little amount of data for training and evaluating deep neural networks in this study, which may have an impact on how well they learn. Because of this, we hope to use explore more with larger image datasets in the future. These computational methods can be used to assist oncologists and specialists in accurately detecting leukaemia. This work will be further investigated to classify all sub-types of cancers from microscopic images as we considered only one type of white blood cancer (ALL), and validating that deep learning could be of aid in diagnosis of various blood cancers.

Acknowledgment

This research did not receive any specific grant from funding agencies in the public, commercial, or not-for-profit sectors.

Conflicts of interest

The authors have no conflicts of interest to declare.

Author's contribution statement

Agughasi Victor Ikechukwu: Conceptualization, investigation, data collection, design, writing - original draft, writing - review and editing, analysis and interpretation of results. **Murali S.:** Study conception, supervision, investigation on challenges and draft manuscript verification.

References

[1] Dong Y, Shi O, Zeng Q, Lu X, Wang W, Li Y, et al. Leukemia incidence trends at the global, regional, and national level between 1990 and 2017. Experimental Hematology & Oncology. 2020; 9(1):1-11.

[2] https://www.webmd.com/cancer/lymphoma/types-and-differences#1. Accessed 26 July 2022.

[3] Perkonigg M, Hofmanninger J, Menze B, Weber MA, Langs G. Detecting bone lesions in multiple myeloma patients using transfer learning. In data driven treatment response assessment and preterm, perinatal, and paediatric image analysis 2018 (pp. 22-30). Springer, Cham.

[4] Thanh TT, Vununu C, Atoev S, Lee SH, Kwon KR. Leukemia blood cell image classification using convolutional neural network. International Journal of Computer Theory and Engineering. 2018; 10(2):54-8.

[5] Kumar D, Jain N, Khurana A, Mittal S, Satapathy SC, Senkerik R, et al. Automatic detection of white blood cancer from bone marrow microscopic images using convolutional neural networks. IEEE Access. 2020; 8:142521-31.

[6] Ianniciello A, Helgason GV. Autophagy in hematopoiesis and leukemogenesis. In autophagy in health and disease 2022 (pp. 125-41). Academic Press.

[7] Liu Y, Long F. Acute lymphoblastic leukemia cells image analysis with deep bagging ensemble learning. In ISBI 2019 C-NMC challenge: classification in cancer cell imaging 2019 (pp. 113-21). Springer, Singapore.

[8] B KA, Kyjenko VM, Zukow W, Popovych IL. Causal neuro-immune relationships at patients with chronic pyelonephritis and cholecystitis. correlations between parameters EEG, HRV and white blood cell count. Open Medicine. 2017; 12(1):201-13.

[9] Fouladi S, Ebadi MJ, Safaei AA, Bajuri MY, Ahmadian A. Efficient deep neural networks for classification of COVID-19 based on CT images: virtualization via software defined radio. Computer Communications. 2021; 176:234-48.

[10] Kassani SH, Kassani PH, Wesolowski MJ, Schneider KA, Deters R. A hybrid deep learning architecture for leukemic B-lymphoblast classification. In 2019 international conference on information and communication technology convergence 2019 (pp. 271-6). IEEE.

[11] Xu L, Tetteh G, Lipkova J, Zhao Y, Li H, Christ P, et al. Automated whole-body bone lesion detection for multiple myeloma on 68Ga-pentixafor PET/CT imaging using deep learning methods. Contrast Media & Molecular Imaging. 2018.

[12] Zhao J, Zhang M, Zhou Z, Chu J, Cao F. Automatic detection and classification of leukocytes using convolutional neural networks. Medical & Biological Engineering & Computing. 2017; 55(8):1287-301.

[13] Abibullaev B, An J, Jin SH, Lee SH, Moon JI. Minimizing inter-subject variability in fNIRS-based

brain–computer interfaces via multiple-kernel support vector learning. Medical Engineering & Physics. 2013; 35(12):1811-8.
[14] Mourya S, Kant S, Kumar P, Gupta A, Gupta R. LeukoNet: DCT-based CNN architecture for the classification of normal versus Leukemic blasts in B-ALL cancer. arXiv preprint arXiv:1810.07961. 2018.
[15] He K, Zhang X, Ren S, Sun J. Deep residual learning for image recognition. In proceedings of the IEEE conference on computer vision and pattern recognition 2016 (pp. 770-8).
[16] He K, Zhang X, Ren S, Sun J. Spatial pyramid pooling in deep convolutional networks for visual recognition. IEEE Transactions on Pattern Analysis and Machine Intelligence. 2015; 37(9):1904-16.
[17] Labati RD, Piuri V, Scotti F. All-IDB: the acute lymphoblastic leukemia image database for image processing. In 2011 IEEE international conference on image processing 2011 (pp. 2045-8). IEEE.
[18] Duggal R, Gupta A, Gupta R, Mallick P. SD-layer: stain deconvolutional layer for CNNs in medical microscopic imaging. In international conference on medical image computing and computer-assisted intervention 2017 (pp. 435-43). Springer, Cham.
[19] Gupta A, Duggal R, Gehlot S, Gupta R, Mangal A, Kumar L, et al. GCTI-SN: geometry-inspired chemical and tissue invariant stain normalization of microscopic medical images. Medical Image Analysis. 2020.
[20] Duggal R, Gupta A, Gupta R, Wadhwa M, Ahuja C. Overlapping cell nuclei segmentation in microscopic images using deep belief networks. In proceedings of the tenth Indian conference on computer vision, graphics and image processing 2016 (pp. 1-8).
[21] Gupta R, Mallick P, Duggal R, Gupta A, Sharma O. Stain color normalization and segmentation of plasma cells in microscopic images as a prelude to development of computer assisted automated disease diagnostic tool in multiple myeloma. Clinical Lymphoma, Myeloma and Leukemia. 2017; 17(1).
[22] Foran DJ, Comaniciu D, Meer P, Goodell LA. Computer-assisted discrimination among malignant lymphomas and leukemia using immunophenotyping, intelligent image repositories, and telemicroscopy. IEEE Transactions on Information Technology in Biomedicine. 2000; 4(4):265-73.
[23] Rehman A, Abbas N, Saba T, Rahman SI, Mehmood Z, Kolivand H. Classification of acute lymphoblastic leukemia using deep learning. Microscopy Research and Technique. 2018; 81(11):1310-7.
[24] Markiewicz T, Osowski S, Marianska B, Moszczynski L. Automatic recognition of the blood cells of myelogenous leukemia using SVM. In proceedings 2005 IEEE international joint conference on neural networks, 2005 (pp. 2496-501). IEEE.
[25] Shafique S, Tehsin S. Acute lymphoblastic leukemia detection and classification of its subtypes using pretrained deep convolutional neural networks. Technology in Cancer Research & Treatment. 2018.
[26] Abd HNH, Mashor MY, Hassan R. Automatic blasts counting for acute leukemia based on blood samples. International Journal of Research and Reviews in Computer Science. 2011; 2(4):971-6.
[27] Wu J, Zeng P, Zhou Y, Olivier C. A novel color image segmentation method and its application to white blood cell image analysis. In international conference on signal processing 2006.
[28] Salihah A, Nasir A, Mustafa N, Fazli N, Nasir M. Application of thresholding technique in determining ratio of blood cells for leukemia detection. Proceedings of the international conference on man-machine systems 2009 (pp.1-6).
[29] Horie Y, Yoshio T, Aoyama K, Yoshimizu S, Horiuchi Y, Ishiyama A, et al. Diagnostic outcomes of esophageal cancer by artificial intelligence using convolutional neural networks. Gastrointestinal Endoscopy. 2019; 89(1):25-32.
[30] Saba T, Khan MA, Rehman A, Marie-sainte SL. Region extraction and classification of skin cancer: aheterogeneous framework of deep CNN features fusion and reduction. Journal of Medical Systems. 2019; 43(9):1-19.
[31] Sekaran K, Chandana P, Krishna NM, Kadry S. Deep learning convolutional neural network (CNN) with Gaussian mixture model for predicting pancreatic cancer. Multimedia Tools and Applications. 2020; 79(15):10233-47.
[32] Zuluaga-gomez J, Al MZ, Benaggoune K, Meraghni S, Zerhouni N. A CNN-based methodology for breast cancer diagnosis using thermal images. Computer Methods in Biomechanics and Biomedical Engineering: Imaging & Visualization. 2021; 9(2):131-45.
[33] Ikechukwu AV, Murali S, Deepu R, Shivamurthy RC. ResNet-50 vs VGG-19 vs training from scratch: a comparative analysis of the segmentation and classification of Pneumonia from chest X-ray images. Global Transitions Proceedings. 2021; 2(2):375-81.
[34] Dabeer S, Khan MM, Islam S. Cancer diagnosis in histopathological image: CNN based approach. Informatics in Medicine Unlocked. 2019.
[35] Ahmed N, Yigit A, Isik Z, Alpkocak A. Identification of leukemia subtypes from microscopic images using convolutional neural network. Diagnostics. 2019; 9(3):1-11.
[36] Genovese A, Hosseini MS, Piuri V, Plataniotis KN, Scotti F. Histopathological transfer learning for acute lymphoblastic leukemia detection. In international conference on computational intelligence and virtual environments for measurement systems and applications 2021 (pp. 1-6). IEEE.
[37] Zolfaghari M, Sajedi H. A survey on automated detection and classification of acute leukemia and WBCs in microscopic blood cells. Multimedia Tools and Applications. 2022; 81(5):6723-53.
[38] Vieira G, Valle ME. Acute lymphoblastic leukemia detection using hypercomplex-valued convolutional neural networks. arXiv preprint arXiv:2205.13273. 2022.

[39] Kasani PH, Park SW, Jang JW. An aggregated-based deep learning method for leukemic B-lymphoblast classification. Diagnostics. 2020; 10(12):1-17.
[40] Bodzas A, Kodytek P, Zidek J. Automated detection of acute lymphoblastic leukemia from microscopic images based on human visual perception. Frontiers in Bioengineering and Biotechnology. 2020.
[41] Alagu S. Automatic detection of acute lymphoblastic leukemia using UNET based segmentation and statistical analysis of fused deep features. Applied Artificial Intelligence. 2021; 35(15):1952-69.
[42] Jiang Z, Dong Z, Wang L, Jiang W. Method for diagnosis of acute lymphoblastic leukemia based on ViT-CNN ensemble model. Computational Intelligence and Neuroscience. 2021.
[43] Granero MA, Hernández CX, Valle ME. Quaternion-valued convolutional neural network applied for acute lymphoblastic leukemia diagnosis. In Brazilian conference on intelligent systems 2021 (pp. 280-93). Springer, Cham.
[44] Wang S, Xia X, Ye L, Yang B. Automatic detection and classification of steel surface defect using deep convolutional neural networks. Metals. 2021; 11(3):1-22.
[45] Simonyan K, Zisserman A. Very deep convolutional networks for large-scale image recognition. arXiv preprint arXiv:1409.1556. 2014.
[46] Rajpurkar P, Irvin J, Zhu K, Yang B, Mehta H, Duan T, et al. Chexnet: radiologist-level pneumonia detection on chest x-rays with deep learning. arXiv preprint arXiv:1711.05225. 2017.
[47] Loey M, Smarandache F, Khalifa NEM. Within the lack of chest COVID-19 X-ray dataset: a novel detection model based on GAN and deep transfer learning. Symmetry. 2020; 12(4):1-19.
[48] Apostolopoulos ID, Mpesiana TA. Covid-19: automatic detection from x-ray images utilizing transfer learning with convolutional neural networks. Physical and Engineering Sciences in Medicine. 2020; 43(2):635-40.
[49] Shafique S, Tehsin S, Anas S, Masud F. Computer-assisted acute lymphoblastic leukemia detection and diagnosis. In international conference on communication, computing and digital systems 2019 (pp. 184-9). IEEE.
[50] Mondal C, Hasan M, Jawad M, Dutta A, Islam M, Awal M, et al. Acute lymphoblastic leukemia detection from microscopic images using weighted ensemble of convolutional neural networks. arXiv preprint arXiv:2105.03995. 2021.

Agughasi Victor Ikechukwu received his Bachelors (BSc) degree from Michael Okpara University of Agriculture Umudike-Nigeria in 2010 and Masters (MSc) degree from Bangalore University, India in 2016 and currently pursuing his Ph.D. in Computer Science from the University of Mysore-India. Since 2019, he is working as a research assistant in the Department of Computer Science and Enginnering, Maharaja Institute of Technology, Mysore-India. He has authored 3 research articles, conducted 7 workshops in deep learning and has an educational YouTube channel where he shares his ideas on python for machine learning. His research interest includes Medical Image Processing, Computer Vision and Deep Learning.
Email: victor.agughasi@gmail.com

Dr. Murali S., received his Bachelors of Engineering BE (E&C) from JMIT Chitradrga in 1988, and M.Tech from MIT Manipal degrees in electronics and communication engineering in 1994 and the Ph.D. degree in computer science from Mysore University, Karnataka, India, in 2002. From 2010 till date, he is a Professor and Dean of research at Maharaja Institute of Technology Mysore. His research interests include distance estimation, camera calibration, digital image processing, computer vision and machine learning applications.
Email: murali@mitmysore.in

Appendix I

S. No.	Abbreviation	Description
1	ALL	Acute Lymphoblastic Leukaemia
2	BMP	Bitmap
3	CADS	Computer Aided Diagnostic System
4	CBC	Complete Blood Count
5	CDSS	Clinical Decision Support System
6	CNN	Convolutional Neural Network
7	CT	Computed Tomography
8	CXR	Chest X-Ray images
9	FN_{all}	False Negative of ALL
10	FP_{all}	False Positive of ALL
11	FPR	False Positive Rate
12	GCS	Global Contrast Stretching
13	GPU	Graphics Processing Unit
14	HSI	Hue, Saturation and Intensity
15	HSV	Hue, Saturation and Value
16	HVN	Hypercomplex-Valued Network
17	ILSVRC 2015	ImageNet Large Scale Visual Recognition
18	LR	Learning Rate
19	M	Momentum
20	MM	Multiple Myeloma
21	PPV	Positive Predictive Value
22	RBC	Red Blood Corpuscles
23	ReLU	Rectified Linear Unit
24	ResNet	Residual Networks
25	ROC	Receiver Operating Curve
26	SOTA	State-of-the-Art
27	SVM	Support Vector Machines
28	TCIA	The Cancer Imaging Institute
29	TN	True Negative
30	TP	True Positive
31	TPR	True Positive Rate
32	TPU	Tensor Processing Unit
33	2D	Two dimensional
34	VGG	Visual Geometry Group Networks
35	WBC	White Blood Corpuscles